Antibiotic action revealed by real-time imaging of the mycobacterial membrane

Michael G. Wuo[1], Charles L. Dulberger[2], Robert A. Brown[3], Alexander Sturm[4], Eveline Ultee[5], Zohar Bloom-Ackermann[4], Catherine Choi[4], Ethan C. Garner[6], Ariane Briegel[5], Deborah T. Hung[4,7,8], Eric J. Rubin[2], Laura L. Kiessling[1]*

Affiliations:

[1]Department of Chemistry, Massachusetts Institute of Technology, Cambridge, MA 02139, USA

[2]Department of Immunology and Infectious Diseases, Harvard T.H. Chan School of Public Health, Boston 02115, MA, USA

[3]Department of Biochemistry of Wisconsin-Madison, Madison WI 53706-1544, USA

[4]Broad Institute of MIT and Harvard, Cambridge, MA 02142, USA

[5]Institute of Biology, University of Leiden, 2333 BE Leiden, Netherlands

[6]Department of Molecular and Cellular Biology, Harvard University, Cambridge, MA 02138 USA

[7]Department of Molecular Biology and Center for Computational and Integrative Biology, Massachusetts General Hospital, Boston, MA, USA

[8]Department of Genetics, Harvard Medical School, Boston, MA, USA

*Corresponding author Email: kiesslin@mit.edu

Abstract: The current understanding of mycobacterial cell envelope remodeling in response to antibiotics is limited. Chemical tools that report on phenotypic changes with minimal cell wall perturbation are critical to gaining insight into this time-dependent phenomenon. Herein we describe a fluorogenic chemical probe that reports on mycobacterial cell envelope assembly in real time. We used time-lapse microscopy to reveal distinct spatial and temporal changes in the mycobacterial membrane upon treatment with frontline antibiotics. Differential antibiotic treatment elicited unique cellular phenotypes, providing a platform for monitoring cell envelope construction and remodeling responses simultaneously. Analysis of the imaging data indicates a role for antibiotic-derived outer membrane vesicles in immune modulation.

Mycobacterial cell envelope biogenesis and remodeling are dynamic processes critical to infectivity and recalcitrance to antibiotics(*1*). Mycolyl arabinogalactan (mAG) is the principal constituent of the cellular envelope and acts as a physical barrier between the bacillus and its environment(*2–4*). Changes in envelope architecture play a critical role in colony morphology, pellicle formation, and drug resistance(*5–7*). Substantial restructuring of the cell envelope as a result of increased production of mycolic acids, changes in arabinogalactan synthesis, and modifications of peptidoglycan crosslinks have been reported to contribute to mechanisms of bacterial persistence and cellular survival(*8–11*). Previous studies have evaluated morphological changes in physical dimensions and DNA compaction after antibiotic treatment (Fig 1A) (*12*). However, these changes alone cannot account for the persistent infections that reestablish following antibiotic treatment. New approaches to evaluate mycobacterial membrane remodeling dynamics under antibiotic stress stand to identify mechanisms of mycobacterial persistence and discover new therapeutic strategies to address the growing threat of mycobacterial antibiotic resistance.

Most frontline antibiotics engage biosynthetic enzymes involved in mycobacterial cell envelope construction. Strategies that report in real-time on mycomembrane dynamics can illuminate how mycobacterial growth, division, and remodeling relate to survival advantages in the bacillus. We recently described a fluorogenic probe, quencher trehalose fluorophore (QTF)(*13*), that reports on the growth of the lipid-rich mycobacterial cell envelope (Fig. 1A). To improve the thermodynamic and hydrolytic stability of the probe, we made a single atom substitution at the trehalose C6-position to generate an amide-containing derivative, N-quencher trehalose fluorophore or N-QTF (Fig. 1B, Supp. Fig. S1, S2). We demonstrate that N-QTF activation in mycobacterial species is mediated by mycolyltransferases Ag85A-C, and this probe localizes to the polar and septal regions (Fig. 1C. Supp Fig. S3) of growing mycobacteria as previously described for QTF. Thus, N-QTF enables selective, real-time visualization of envelope biogenesis.

We leveraged N-QTF to examine spatial and temporal fluorogenic phenotypes in response to antibiotic stress. We first determined how antibiotic treatment influenced fluorescence resulting from N-QTF processing. Using a time-course fluorescence assay, we subjected *Mycobacterium smegmatis* (*Msmeg*) to frontline *Mycobacterium* tuberculosis (*Mtb*) antibiotics ethambutol (EMB), rifampicin (RIF), and isoniazid (INH) at 12.5 μg/mL (low, sub-MIC) and 50 μg/mL (high, super-MIC) concentrations. The bulk fluorescence measured over six hours (two doubling times, Supp Fig. S4) tracked with antibiotic concentration with a higher fluorescent signal at higher antibiotic concentration (Fig. 1D). A linear correlation of fluorescence and OD600 was observed for all treatment conditions, suggesting that the bacteria could grow and multiply under the assay conditions during this short, early period of observation (Supp. Fig. S4). Of the frontline antibiotics, ethambutol (EMB)-treated cells exhibited the largest fluorescence increase at high concentrations and largest fluorescence decrease at low concentrations relative to untreated control. Rifampicin (RIF)-treated cells had the smallest relative fluorescence change, while isoniazid (INH) treatment had an intermediate response. These data suggest *Msmeg* increases lipid remodeling activity under antibiotic stress and that each anti-mycobacterial agent elicits a distinct cell membrane response.

EMB inhibits the arabinosyltransferases EmbA-C(*14*). These enzymes generate the cell envelope arabinan layer, to which the lipid-rich mycolic acid layer is appended. Prior studies indicate ethambutol treatment results in an intracellular accumulation and secretion of trehalose mycolates and mycolic acids in the culture media(*15*, *16*). In one study, EMB treatment induced increased expression of the polar scaffolding protein DivIVA(*17*), a fulcrum for the organization of the polar elongation complex, elongasome. This investigation recorded active growth at the cellular poles; paradoxically, the level of mycolic acid at the cellular poles appeared to be reduced (*17*). We reasoned that these counterintuitive results likely stem from the non-specific fluorescent dye used to monitor mycolic acid changes. The fluorescence of such dyes depends on the hydrophobicity of the region; therefore, they cannot report on dynamic

remodeling. We postulated that N-QTF could report on lipid restructuring in real time. Using time-lapse imaging under microfluidic control, we continuously supplied N-QTF to *Msmeg* and flowed either vehicle or EMB antibiotic (10 μg/mL) into the culture chamber at defined time points (Fig. 2A-C, Movies S1-S4). Changes in fluorescence localization were monitored over time. After one doubling time, EMB-treated *Msmeg* showed bright fluorescence localization to the bacillus' polar regions. The observed phenotype increased over time, and after 16 hours, we detected ejection of the mycomembrane lipids at these sites. These data suggest that the cell pole is more fluid than previously described, a property that explains why non-specific fluorescent dyes could not report on the lipid changes revealed by N-QTF. These new findings underscore the importance of capturing the dynamics of lipid remodeling under antibiotic treatment, as spatiotemporal resolution provides mechanistic insight into changes in cell wall biosynthetic pathways.

We reasoned that other cell wall biosynthesis inhibitors might exhibit similar lipid localization phenotypes. The bactericidal frontline antibiotic INH targets the enoyl reductase InhA involved in cell envelope construction and perturbs the available mycolic acid lipid pool. Time-lapse imaging revealed a delayed fluorogenic phenotype after one doubling time (Fig 2D). The fluorescence appeared to be dispersed throughout the cell membrane, supporting the known lytic mechanism of action of INH at a super-MIC concentration(*18*). Cell surface blebbing followed by membrane shredding has been reported to precede lytic activity in INH-treated *Msmeg*(*19*). Unexpectedly, we observed that EMB and INH, which both target cell envelope biosynthesis, did not produce similar phenotypes, suggesting differential drug mechanism of action results in altered lipid localization phenotypes in mycobacterial membranes.

We next tested whether antibiotics that block processes that do not directly impact cell envelope biogenesis would afford mycomembrane perturbations. To this end, we treated *Msmeg* with RIF, an antibiotic that engages bacterial RNA polymerase and blocks the initiation of RNA synthesis. Time-lapse imaging revealed the RIF treatment promoted the appearance of outer

membrane vesicles (OMVs) (Fig. 2E). This phenotype was absent in either EMB- and INH-treated samples, indicating a RIF-specific stress response. Bacteria, including *Mtb,* actively release outer membrane vesicles in the absence of stress(*20–22*); however, enhanced OMV production following antibiotic treatment had not been previously observed. Imaging of N-QTF in RIF treated cells reveals previously uncharacterized cell wall activity upon inhibition of bacterial transcription.

To gather additional insight into the varied antibiotic phenotypes observed in fluorescence microscopy, we used cryo-transmission electron microscopy (cryo-TEM). Guided by our dynamic phenotypic profiling, we treated *Msmeg* with EMB, INH, or RIF at sublethal doses. After four hours of antibiotic treatment, cryo-TEM images revealed dramatic differences, analogous to those observed in time-lapse microscopy (Fig. 2F). EMB-treated bacteria showed lipid droplet accumulation at the cell poles. INH treatment caused lipid accumulation along the cell length and polar regions. RIF exposure resulted in the appearance of phosphate and lipid-rich subcellular bodies(*23*) appearing throughout the bacillus, suggesting a priming step that occurs before OMV release. These data indicate that N-QTF does not itself contribute to the observed phenotypes but strictly acts as a reporter of cell remodeling.

The distinct OMV phenotype observed in RIF-treated mycobacteria was intriguing, as cryo-TEM could not capture this time-dependent phenotype, and previous studies indicate that secreted mycobacterial OMVs can modulate host immunity through TLR agonism. In this way, OMVs can help Mtb subvert immune surveillance by macrophages(*20*). We posited that the OMV phenotype observed in RIF-treated mycobacteria might provide insight into the recent rise in *Mtb* resistance to RIF. Indeed, RIF-treated infected macrophages can give rise to RIF-resistant *Mtb* with modified lipid envelopes (*24*). To query how mycobacterial OMVs under antibiotic treatment modulate host immune response, we isolated OMVs from the supernatant of DMSO vehicle- or RIF-treated *Mtb* and used them to stimulate human blood monocyte-derived macrophages (Fig. 3A). We compared the responses to that of lipopolysaccharide from

Gram-negative *Escherichia coli*, a potent stimulant of the human immune system. RT-qPCR analysis of primary human macrophages incubated with OMVs from DMSO-treated *Mtb* afforded an increase in the expression of primary proinflammatory cytokines. Notably, treatment of primary human macrophages with OMVs from RIF-treated *Mtb* decreased proinflammatory cytokine expression relative to OMVs from vehicle-treated *Mtb*. To further explore how a range of frontline antibiotics influence OMV-mediated immune modulation, we isolated OMVs from EMB-treated *Mtb*. The proinflammatory cytokine response from EMB OMVs was similar to that of the DMSO OMV control across the proinflammatory cytokines IL-1b, IL-6, and IL12b (Fig 3C). These data indicate that the distinct phenotypes observed in our imaging studies have different consequences on immune activation. The data suggest that cell envelope remodeling by Mtb in response to RIF treatment can help evade host defense.

OMVs help *Mtb* and other bacteria deliver biomolecules at a high effective concentration. To explore the molecular basis of macrophage modulation by antibiotic-treated OMVs, we performed a targeted metabolomics analysis of 167 metabolites (Fig. 3D)(*25*). The data indicated a significant upregulation in adenosine pathway metabolites in RIF OMVs over DMSO OMVs. The largest fold-change was observed for cyclic AMP (cAMP), suggesting a link between intra-membrane vesicle cyclic AMP concentration and immune modulation. Since EMB OMVs did not significantly activate the proinflammatory macrophage response, we hypothesized that cAMP would not be present in EMB OMV metabolites. Consistent with this hypothesis, a targeted metabolomics analysis of EMB OMVs showed no increase in cAMP or other adenosine metabolites (Fig. 3D). Changes in intramacrophage cAMP levels have been observed in *Mtb* infection. Increases in cAMP can dampen macrophage signaling through protein kinase A and the cAMP response-element binding protein pathways(*26–28*); however, cAMP's presence in OMVs had not been examined. The delivery of high local concentrations of encapsulated cAMP in response to RIF may allow *Mtb* to control host macrophage immune responses, suggesting a mechanism for bacterial survival and subsequent host tolerance.

The mycobacterial membrane grants *Mtb* recalcitrance to antimicrobials. How the mycomembrane dynamically remodels in response to antibiotic stress was poorly understood. By leveraging a substrate mimic of the enzymes that control mycomembrane remodeling, we investigated changes in membrane phenotypes from frontline antibiotic treatment without genetic manipulation. The critical observation that the spatial and temporal localization of the lipids is dependent on an antibiotic's mechanism of action highlights the utility of our approach. The secretion of OMVs from RIF-treated mycobacteria was unprecedented and suggests bacteria modulate the host immune environment as collateral damage to their stress response (Supp. Fig. S5). Our findings indicate that consideration of the consequences of bacterial treatment on host immune responses could yield more effective strategies for antibiotic targeting of *Mtb*. Last, we demonstrate how the mycomembrane can be leveraged to report on the biology of existing antibiotics and discover new mechanisms of action.

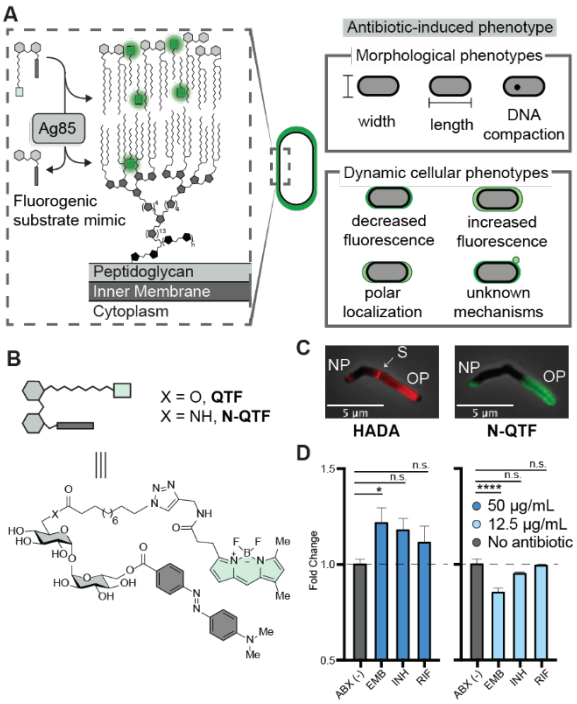

Figure 1. Analysis of N-QTF, a fluorogenic, real-time reporter of mycolyltransferase activity. (A) The fluorogenic substrate (QTF or N-QTF, B) is activated by the Ag85 enzyme complex and serves as a reporter of dynamic antibiotic-induced cellular phenotypes. (B) The fluorogenic probes, QTF and N-QTF, mimic critical features of trehalose monomycolate, the natural substrate of Ag85. (C) Fluorescence labeling of *M. smegmatis* with HADA (left) or N-QTF (right). NP: new pole OP: old pole S: septum (D) Bulk fluorescence measurements show concentration-dependent N-QTF activation differences upon treatment with frontline antibiotics at 50 µg/mL (left, blue) and 12.5 µg/mL (right, light blue). (Ordinary oneway-ANOVA ****$p \leq 0.0001$, ***$p \leq 0.001$, **$p \leq 0.01$, *$p \leq 0.05$ and non-significant >0.05). Data shown are the average of triplicate samples ± SEM in triplicate and representative of two independent experiments.

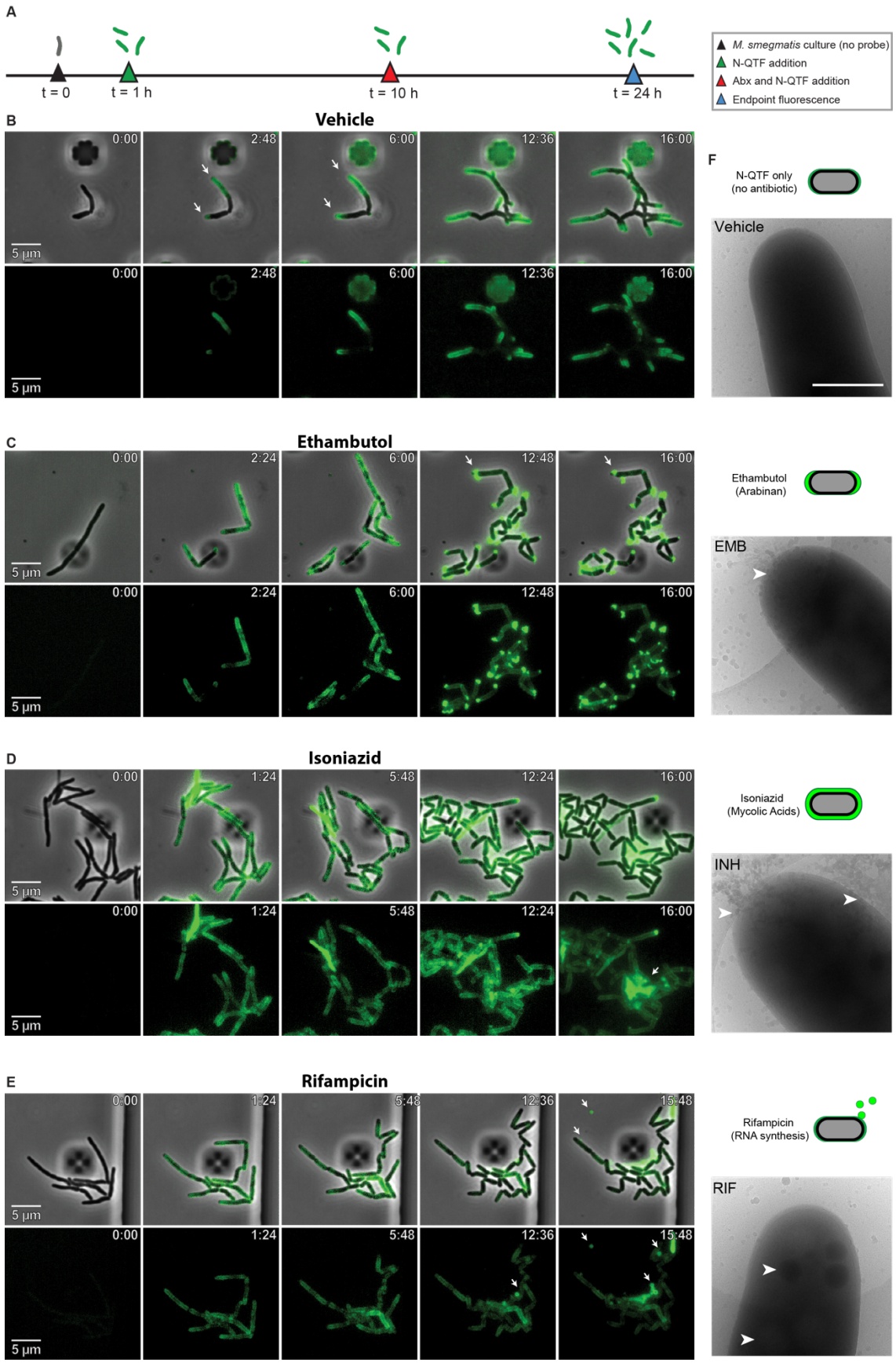
A
t = 0
t = 1 h
t = 10 h
t = 24 h
M. smegmatis culture (no probe)
N-QTF addition
Abx and N-QTF addition
Endpoint fluorescence
B
Vehicle
0:00
2:48
6:00
12:36
16:00
5 µm
C
Ethambutol
0:00
2:24
6:00
12:48
16:00
5 µm
D
Isoniazid
0:00
1:24
5:48
12:24
16:00
5 µm
E
Rifampicin
0:00
1:24
5:48
12:36
15:48
5 µm
F
N-QTF only
(no antibiotic)
Vehicle
Ethambutol
(Arabinan)
EMB
Isoniazid
(Mycolic Acids)
INH
Rifampicin
(RNA synthesis)
RIF

Figure 2. Antibiotic-specific phenotypes from fluorescence and superimposed phase imaging of *Msmeg*. (A) N-QTF and antibiotic treatment timeline used to monitor antibiotic phenotypes. (B) Combined microfluidics and time-lapse microscopy were used to assess antibiotic phenotypes relative to vehicle control following (C) EMB treatment, (D) INH treatment, (E) RIF-treatment. (F) Cryo-transmission electron microscopy after four hours of exposure. Arrows indicate antibiotic phenotypes. Images are presented for vehicle, or treatment with EMB, INH, or RIF. Data are representative of two individual experiments.

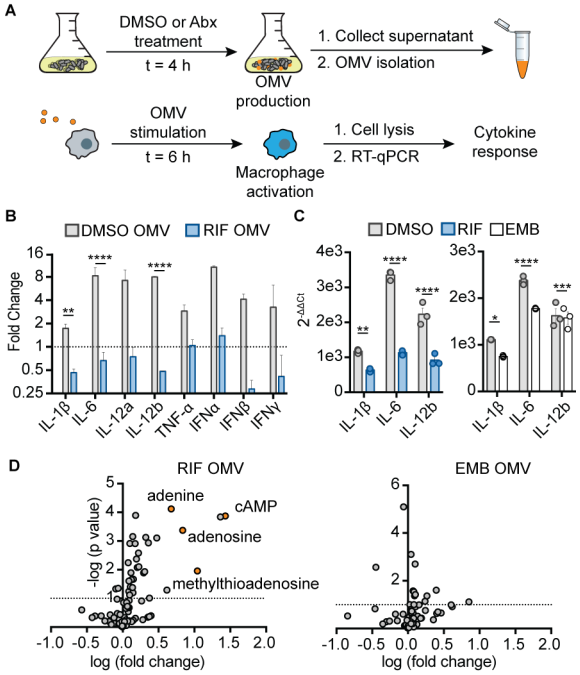

Figure 3. Assessment of human macrophage responses to OMVs from *Mtb*. (A) Schematic depiction of experimental workflow. OMVs were isolated from *Mtb* following treatment with DMSO, RIF, or EMB and exposed to human macrophages. Cytokine expression was measured following macrophage stimulation with purified OMVs. (B) RT-qPCR analysis of macrophage cytokine expression in response to RIF OMVs relative to LPS control. (C) A comparison of macrophage cytokine expression elicited by RIF OMVs compared to that from EMB OMVs. (Two-way ANOVA ****$p \leq 0.0001$, ***$p \leq 0.001$, **$p \leq 0.01$, *$p \leq 0.05$ and non-significant >0.05). (D) Untargeted metabolomics of polar metabolites present in OMVs from RIF- or EMB-treated *Mtb*. Data are representative of two independent experiments.

References

1. C. L. Dulberger, E. J. Rubin, C. C. Boutte, The mycobacterial cell envelope - a moving target. *Nat. Rev. Microbiol.* **18**, 47–59 (2020).

2. M. Jankute, J. A. G. Cox, J. Harrison, G. S. Besra, Assembly of the Mycobacterial Cell Wall. *Annu. Rev. Microbiol.* **69**, 405–423 (2015).

3. P. J. Brennan, Structure, function, and biogenesis of the cell wall of Mycobacterium tuberculosis. *Tuberc. Edinb. Scotl.* **83**, 91–97 (2003).

4. G. S. Besra, K. H. Khoo, M. R. McNeil, A. Dell, H. R. Morris, P. J. Brennan, A new interpretation of the structure of the mycolyl-arabinogalactan complex of Mycobacterium tuberculosis as revealed through characterization of oligoglycosylalditol fragments by fast-atom bombardment mass spectrometry and 1H nuclear magnetic resonance spectroscopy. *Biochemistry*. **34**, 4257–4266 (1995).

5. J. Liu, C. E. Barry, G. S. Besra, H. Nikaido, Mycolic acid structure determines the fluidity of the mycobacterial cell wall. *J. Biol. Chem.* **271**, 29545–29551 (1996).

6. A. Venugopal, R. Bryk, S. Shi, K. Rhee, P. Rath, D. Schnappinger, S. Ehrt, C. Nathan, Virulence of Mycobacterium tuberculosis depends on lipoamide dehydrogenase, a member of three multienzyme complexes. *Cell Host Microbe*. **9**, 21–31 (2011).

7. J. M. Chen, G. J. German, D. C. Alexander, H. Ren, T. Tan, J. Liu, Roles of Lsr2 in colony morphology and biofilm formation of Mycobacterium smegmatis. *J. Bacteriol.* **188**, 633–641 (2006).

8. K. J. Kieser, E. J. Rubin, How sisters grow apart: mycobacterial growth and division. *Nat. Rev. Microbiol.* **12**, 550–562 (2014).

9. S. Bhamidi, L. Shi, D. Chatterjee, J. T. Belisle, D. C. Crick, M. R. McNeil, A bioanalytical method to determine the cell wall composition of Mycobacterium tuberculosis grown in vivo. *Anal. Biochem.* **421**, 240–249 (2012).

10. M. Jain, C. J. Petzold, M. W. Schelle, M. D. Leavell, J. D. Mougous, C. R. Bertozzi, J. A. Leary, J. S. Cox, Lipidomics reveals control of Mycobacterium tuberculosis virulence lipids via metabolic coupling. *Proc. Natl. Acad. Sci. U. S. A.* **104**, 5133–5138 (2007).

11. A. A. Pohane, C. R. Carr, J. Garhyan, B. M. Swarts, M. S. Siegrist, Trehalose Recycling Promotes Energy-Efficient Biosynthesis of the Mycobacterial Cell Envelope. *mBio*. **12** (2021), doi:10.1128/mBio.02801-20.

12. T. C. Smith, K. M. Pullen, M. C. Olson, M. E. McNellis, I. Richardson, S. Hu, J. Larkins-Ford, X. Wang, J. S. Freundlich, D. M. Ando, B. B. Aldridge, Morphological profiling of tubercle bacilli identifies drug pathways of action. *Proc. Natl. Acad. Sci. U. S. A.* **117**, 18744–18753 (2020).

13. H. L. Hodges, R. A. Brown, J. A. Crooks, D. B. Weibel, L. L. Kiessling, Imaging mycobacterial growth and division with a fluorogenic probe. *Proc. Natl. Acad. Sci. U. S. A.* **115**, 5271–5276 (2018).

14. L. Zhang, Y. Zhao, Y. Gao, L. Wu, R. Gao, Q. Zhang, Y. Wang, C. Wu, F. Wu, S. S. Gurcha, N. Veerapen, S. M. Batt, W. Zhao, L. Qin, X. Yang, M. Wang, Y. Zhu, B. Zhang, L. Bi, X. Zhang, H. Yang, L. W. Guddat, W. Xu, Q. Wang, J. Li, G. S. Besra, Z. Rao, Structures of cell wall arabinosyltransferases with the anti-tuberculosis drug ethambutol. *Science*. **368**, 1211–1219 (2020).

15. J. O. Kilburn, K. Takayama, Effects of ethambutol on accumulation and secretion of trehalose mycolates and free mycolic acid in Mycobacterium smegmatis. *Antimicrob. Agents Chemother*. **20**, 401–404 (1981).

16. K. Mikusová, R. A. Slayden, G. S. Besra, P. J. Brennan, Biogenesis of the mycobacterial cell wall and the site of action of ethambutol. *Antimicrob. Agents Chemother*. **39**, 2484–2489 (1995).

17. K. Schubert, B. Sieger, F. Meyer, G. Giacomelli, K. Böhm, A. Rieblinger, L. Lindenthal, N. Sachs, G. Wanner, M. Bramkamp, The Antituberculosis Drug Ethambutol Selectively Blocks Apical Growth in CMN Group Bacteria. *mBio*. **8**, e02213-16.

18. M. Elitas, Isoniazid Killing of Mycobacterium smegmatis NADH Pyrophosphatase Mutant at Single-Cell Level using Microfluidics and Time-Lapse Microscopy. *Sci. Rep*. **7**, 10770 (2017).

19. C. Vilchèze, H. R. Morbidoni, T. R. Weisbrod, H. Iwamoto, M. Kuo, J. C. Sacchettini, W. R. Jacobs, Inactivation of the inhA-encoded fatty acid synthase II (FASII) enoyl-acyl carrier protein reductase induces accumulation of the FASI end products and cell lysis of Mycobacterium smegmatis. *J. Bacteriol*. **182**, 4059–4067 (2000).

20. R. Prados-Rosales, A. Baena, L. R. Martinez, J. Luque-Garcia, R. Kalscheuer, U. Veeraraghavan, C. Camara, J. D. Nosanchuk, G. S. Besra, B. Chen, J. Jimenez, A. Glatman-Freedman, W. R. Jacobs, S. A. Porcelli, A. Casadevall, Mycobacteria release active membrane vesicles that modulate immune responses in a TLR2-dependent manner in mice. *J. Clin. Invest*. **121**, 1471–1483 (2011).

21. T. Nagakubo, N. Nomura, M. Toyofuku, Cracking Open Bacterial Membrane Vesicles. *Front. Microbiol*. **10**, 3026 (2020).

22. M. Toyofuku, N. Nomura, L. Eberl, Types and origins of bacterial membrane vesicles. *Nat. Rev. Microbiol*. **17**, 13–24 (2019).

23. L. R. Comolli, M. Kundmann, K. H. Downing, Characterization of intact subcellular bodies in whole bacteria by cryo-electron tomography and spectroscopic imaging. *J. Microsc*. **223**, 40–52 (2006).

24. C. Genestet, E. Hodille, A. Barbry, J.-L. Berland, J. Hoffmann, E. Westeel, F. Bastian, M. Guichardant, S. Venner, G. Lina, C. Ginevra, F. Ader, S. Goutelle, O. Dumitrescu, Rifampicin exposure reveals within-host Mycobacterium tuberculosis diversity in patients with delayed culture conversion. *PLOS Pathog*. **17**, e1009643 (2021).

25. C. Williams, M. Palviainen, N.-C. Reichardt, P. R.-M. Siljander, J. M. Falcón-Pérez, Metabolomics Applied to the Study of Extracellular Vesicles. *Metabolites*. **9**, 276 (2019).

26. N. Agarwal, G. Lamichhane, R. Gupta, S. Nolan, W. R. Bishai, Cyclic AMP intoxication of macrophages by a Mycobacterium tuberculosis adenylate cyclase. *Nature*. **460**, 98–102 (2009).

27. G. Bai, G. S. Knapp, K. A. McDonough, Cyclic AMP signalling in mycobacteria: redirecting the conversation with a common currency. *Cell. Microbiol.* **13**, 349–358 (2011).

28. Y. Chung, V. Pasquinelli, J. O. Jurado, X. Wang, N. Yi, P. F. Barnes, V. E. Garcia, B. Samten, Elevated Cyclic AMP Inhibits Mycobacterium tuberculosis-Stimulated T-cell IFN-γ Secretion Through Type I Protein Kinase A. *J. Infect. Dis.* **217**, 1821–1831 (2018).

29. K. Birsoy, T. Wang, W. W. Chen, E. Freinkman, M. Abu-Remaileh, D. M. Sabatini, An Essential Role of the Mitochondrial Electron Transport Chain in Cell Proliferation Is to Enable Aspartate Synthesis. *Cell*. **162**, 540–551 (2015).

30. D. H. Anderson, G. Harth, M. A. Horwitz, D. Eisenberg, An interfacial mechanism and a class of inhibitors inferred from two crystal structures of the Mycobacterium tuberculosis 30 kDa major secretory protein (Antigen 85B), a mycolyl transferase. *J. Mol. Biol.* **307**, 671–681 (2001).

31. L. Favrot, A. E. Grzegorzewicz, D. H. Lajiness, R. K. Marvin, J. Boucau, D. Isailovic, M. Jackson, D. R. Ronning, Mechanism of inhibition of Mycobacterium tuberculosis antigen 85 by ebselen. *Nat. Commun.* **4**, 2748 (2013).

Supplementary Materials for

Antibiotic action revealed by real-time imaging of the mycobacterial membrane

Michael G. Wuo[1], Charles L. Dulberger[2], Robert A. Brown[3], Alexander Sturm[4], Eveline Ultee[5], Zohar Bloom-Ackermann[4], Catherine Choi[4], Ethan C. Garner[6], Ariane Briegel[5], Deborah T. Hung[4,7,8], Eric J. Rubin[2], Laura L. Kiessling[1]*

Affiliations:

[1]Department of Chemistry, Massachusetts Institute of Technology, Cambridge, MA 02139, USA

[2]Department of Immunology and Infectious Diseases, Harvard T.H. Chan School of Public Health, Boston 02115, MA, USA

[3]Department of Biochemistry of Wisconsin-Madison, Madison WI 53706-1544, USA

[4]Broad Institute of MIT and Harvard, Cambridge, MA 02142, USA

[5]Institute of Biology, University of Leiden, 2333 BE Leiden, Netherlands

[6]Department of Molecular and Cellular Biology, Harvard University, Cambridge, MA 02138 USA

[7]Department of Molecular Biology and Center for Computational and Integrative Biology, Massachusetts General Hospital, Boston, MA, USA

[8]Department of Genetics, Harvard Medical School, Boston, MA, USA

*Corresponding author. Email: kiesslin@mit.edu

This PDF file includes:

Materials and Methods
Supplementary Text
Figs. S1 to S5
Tables S1 to S2
Captions for Movies S1 to S4
References

Materials and Methods

General Information for Synthetic Methods and Materials

All reagents for synthetic starting materials, buffers, and antibiotics were used as received from commercial manufacturers, unless otherwise noted. Organic solvents were purified according to published method guidelines (1). Water was purified using a Millipore Milli-Q Integral Water Purification system. All reactions were conducted under an intert nitrogen atmosphere in oven dried glassware unless otherwise stated. Analytical thin layer chromatography (TLC) was carried out on E. Merck (Darmstadt) TLC plates pre-coated with silica gel 60 F254 (250 μm layer thickness). Analyte visualization was accomplished using a UV lamp or by charring with phosphomolybdic acid solution. Flash column chromatography was performed with Silicycle flash silica gel (40–63 μm, 60 Å pore size) using the quoted eluent. 1H and 13C nuclear magnetic resonance (NMR) spectra were recorded on a 400 MHz spectrometer (acquired at 400 MHz for 1H NMR and 101 MHz for 13C NMR), or a 500 MHz spectrometer (acquired at 500 MHz for 1H NMR and 126 MHz for 13C NMR). NMR chemical shifts are reported as follows: chemical shift (δ ppm), multiplicity (s = singlet, d = doublet, t = triplet, q = quartet, p = quintet, or some combination thereof. Chemical shifts are reported relative to residual solvent peaks in parts per million ($CDCl_3$: 1H, 7.27, 13C, 77.23; CD_3OD: 1H, 3.31, 13C, 49.15). Coupling constants (J) are reported in Hertz (Hz) and rounded to the nearest 0.1 Hz. High-resolution mass spectra (HRMS) were obtained on an electrospray ionization-time of flight (ESI-TOF) Micromass LCT mass spectrometer.

Bacterial strain selection and culture conditions

Mycobacterial species *M. smegmatis* mc2155, *M. marinum* BAA-535, and *M. tuberculosis* H37Rv were grown with shaking at 37°C in Middlebrook 7H9 broth (BD, Franklin Lake, NJ) with 0.2% (v/v) glycerol, 0.05% (v/v) Tween-80 with or without OADC supplement (Sigma-Aldrich).

Time-dependent fluorescence assays

Mycobacterial species *M. smegmatis* mc2155, *M. marinum* BAA-535, and *M. tuberculosis* H37Rv were grown to OD600 = 1. Strains were diluted to OD600=0.2. Reactions were initiated by the addition of N-QTF to a final volume of 50 μL per well (n=3). Relative fluorescence units were measured at ex/em 485/525 and read every 15 minutes for two doubling times (t=6 hours) at 37°C.

Purification of *M. tb* Ag85 mycolyltransferases

Mtb Ag85A, Ag85B, and Ag85C were obtained through BEI Resources, NIAID, NIH: Purified native protein from *M. tb*. H37Rv antigen 85A (fbpA, Rv3804c, cat. No: NR-14856), antigen 85B (fbpB, Rv1886c, cat. No: NR-14857), and antigen 85C (fbpD, Rv3803, cat no: NR-14858). Upon receipt, lyophilized native Ag85 proteins were thawed and suspended in aqueous 1xPBS buffer (Gibco cat no:10010023) to a concentration of 10 μM for storage at –20 °C. M. tb. Ag85A–C proteins were thawed and used as needed.

Kinetic assays with *M. tb*. Ag85A-C mycolyltransferases

A flat, clear bottom 96-well black polystyrene microplate (Greiner, cat no: 655097) was used to measure time-dependent N-QTF activation with 5 μM N-QTF with a fixed concentration (1 μM) of each Ag85 isoform in 1x PBS pH 7.4. Reactions were initiated by the addition of N-QTF to a final volume of 50 μL per well (n=3). Relative fluorescence units were measured at ex/em 485/525 and read every 30 seconds for one hour at 37°C.

Fluorescence microscopy

Mycobacterial species *M. smegmatis* mc2155, M. marinum BAA-535, and M. tuberculosis H37Rv were grown to OD600 = 1 in either Middlebrook 7H9 or 7H9 +OADC supplement 0.2% glycerol, 0.05% Tween-80. Strains were diluted to OD600=0.2 and N-QTF was added at final concentration 2.5 uM in 1 mL of liquid culture. 10 uL of culture was removed after 24 hours and placed on a glass microscope slide with polylysine-coated cover slips. Slips were sealed and imaged on a Cell Discoverer7 at 100x

magnification. Visualization of N-QTF was performed and monitored at ex/em 488/525 nm. Imaging processing was performed using ImageJ FIJI software.

Antibiotic-dependent N-QTF incorporation
A flat, clear bottom 96-well black polystyrene microplate (Greiner, cat no: 655097) was used to measure time-dependent N-QTF (1 μM) activation with frontline antibiotic treatment to *M. smegmatis* mc2155. EMB, INH, or RIF was used to treat *M. smegmatis* at OD600 = 0.2 at either 50 μg/mL or 12.5 μg/mL (n=3). Relative fluorescence units were measured at ex/em 485/525 and read every 15 minutes for two doubling times (t=6 hours) at 37°C.

Timelapse microscopy
M. smegmatis were grown to mid-log and diluted to OD600 of 0.3. Cells were loaded into a CellASIC (cat no: B04A) plate under constant microfluidic flow with 7H9 medium in a 37°C chamber and allowed to grow in chamber for one hour. 7H9 medium supplemented with N-QTF (1 μM) was flowed into the chamber for six hours before switching media to N-QTF with and without antibiotic (10 μg/mL). Images were acquired every 15 min on an inverted Nikon TI-E microscope using a 60× objective. Cells were imaged using phase contrast and ex/em at 488/525 nm.

Cryo-transmission electron microscopy
Cells were cultured to mid-log in complete 7H9 with and without frontline antibiotic treatment at 10 μg/mL for four hours at 37°C. After four hours, cells were concentrated 50-fold by pelleting by centrifugation and resuspending in a 50-fold smaller volume. Concentrated cells were plunge-frozen in liquid ethane using an automated Leica EM GP system (Leica Microsystems) using R2/2 200 mesh grids (Quantifoil) and imaged using a Talos 120 kV cryo-transmission electron microscope.

Monocyte-derived macrophage differentiation and purification
Adult human peripheral blood was acquired from Research Blood Components, LLC (Boston, MA, USA) under IRB approved protocol. Monocytes were isolated from whole blood by negative selection using RosetteSep human monocyte enrichment cocktail following the manufacturer's protocol (StemCell Technologies). Using density gradient medium (Lymphoprep) monocytes were isolated and differentiated into macrophages in the presence of GM-CSF (100 ng/mL) (R&D Systems) in 1640 RPMI + 5% FBS +P/S media for 6 to 7 days

Outermembrane vescicle isolation
M.tb. H37Rv (500 mL) cultures were treated with DMSO, EMB or RIF at 15 ug/mL final concentration for six hours at 37°C. Supernatant was centrifuged at 38,000xg in a JA16.25 (Beckman Coulter) for 3 hours at 4°C. After centrifugation, the supernatant was removed and the pellet was resuspended in 10 mM HEPES 150 mM NaCl pH 7.2. OMV concentration as normalized using absorbance at 280 nm and aliquoted into 100 μL samples and stored at -20°C.

OMV stimulation assay and Quantitative Real-Time PCR.
Vehicle, EMB or RIF OMVs were added to wells containing 500 μL of 750,000 cells/mL and incubated at 37°C for 6 hours. After 6 hours, supernatant was removed, and washed with 2x Cold 1xPBS (1 mL). Trizol reagent (400 μL) was added to the stimulation well. The supernatant was removed at 300 μL of trizol was added. Total RNA was extracted with Trizol using Direct-zol RNA kits (Zymo Research). cDNA was generated by using an iScript cDNA synthesis kit (BioRad), and PCR amplification was performed in the presence of SYBR green (BioRad) in a CFX96 real-time PCR detection system (BioRad). Specific primers were designed using the PrimerQuest tool (Integrated DNA Technologies, Inc., Supplementary Table 1). Expression of specific genes was normalized to GAPDH expression (ΔCt), and expression fold change was calculated using the delta Ct method (2−(ΔCt Stim-ΔCt Unstim)) and normalized to LPS (50 μg).

Polar metabolite isolation
OMV samples from DMSO, EMB, and RIF-treated conditions were extracted to analyze the metabolite composition within them. In an microcentrifuge tube, OMVs (100 μL, n=3) were resuspended in 300 μL of LC/MS grade methanol containing a mixture of 17 isotope-labeled amino acids (200 nM, Cambridge

Isotope Laboratories, MSK-A2-1.2). To this solution, LC/MS grade water (150 µL) was added to each tube. Ice cold amylenes-free chloroform (200 µL) was added to each sample. The sample was vortexed at 4C for 1 minute and centrifuged for 10 minutes at 13,000xg at 4C. The top aqueous layer was removed and allowed to dry under N2 stream overnight. Dried Extracts were stored at -80C until run.

Targeted metabolomics

LC/MS was used to profile and quantify the polar metabolite contents of OMVs from DMSO, EMB, or RIF-treated M.tb.LC/MS-based analyses were performed as described previously(*29*) on a QExactive benchtop orbitrap mass spectrometer equipped with an Ion Max source and a HESI II probe coupled to a Dionex UltiMate 3000 UPLC system (Thermo Fisher Scientific). Metabolite sample (5 µL) was injected onto a ZIC-pHILIC 2.1 × 150 mm (5 µm particle size) column (EMD Millipore). Buffer A was 20 mM ammonium carbonate, 0.1% ammonium hydroxide; buffer B was acetonitrile. A flow rate of 0.150 ml/min was used for the chromatographic gradient. 0–20 min: linear gradient from 80% to 20% B; 20–20.5 min: linear gradient from 20% to 80% B; 20.5–28 min: hold at 80% B. The mass spectrometer was operated in full-scan, polarity switching mode with the spray voltage set to 3.0 kV, the heated capillary held at 275°C, and the HESI probe held at 350°C. The sheath gas flow was set to 40 units, the auxiliary gas flow was set to 15 units, and the sweep gas flow was set to 1 unit. The MS data acquisition was performed in a range of 70–1000 m/z, with the resolution set at 70,000, the AGC target at 10^6, and the maximum injection time at 80 ms. XCalibur QuanBrowser 2.2 (Thermo Fisher Scientific) was used for metabolite identification and quantification using a 10 ppm mass accuracy window and 0.5 min retention time window compared to authentic metabolite standards. Within-batch mass deviation was typically < 0.0005 Da, and retention time deviation was < 0.25 min. In each sample, the raw peak area for each metabolite was divided by the raw peak area of the relevant isotope-labeled internal standard to calculate the relative abundance.

Detailed synthetic procedures

Synthesis of 6-O-(15-[BODIPY-FL]-pentadeconyl)-6'-NH-DABCYL- α,α-trehalose/N-QTF **1** (See Figure S1 for overall route)

Dowex-50WX8-200 ion exchange resin (32 mg) was added to a solution of compound 5 (7.1 mg, 0.0044 mmol) in methanol (1.25 mL) and stirred at rt for 1 hr. The resin was removed by filtration and washed with methanol. The filtrate was concentrated under reduced pressure. Purification of the resulting residue by column chromatography (SiO_2, 10→15% MeOH/CH_2Cl_2) afforded the title compound 1 (3.24 mg, 62%) as an orange solid: R_f = 0.20 (10% MeOH/CH_2Cl_2); ^{1}H NMR (500 MHz, CD_3OD) δ 7.97 – 7.95 (m, 2H), 7.88 – 7.85 (m, 4H), 7.74 (s, 1H), 7.42 (s, 1H), 6.98 (d, J = 4.0 Hz, 1H), 6.86 – 6.84 (m, 2H), 6.30 (d, J = 4.0 Hz, 1H), 6.22 (s, 1H), 5.10 (t, J = 4.1 Hz, 2H), 4.61 (dd, J = 11.9, 2.1 Hz, 1H), 4.44 (dd, J = 11.8, 5.4 Hz, 1H), 4.41 (s, 2H), 4.39 (dd, J = 11.9, 2.2 Hz, 1H), 4.32 (t, J = 7.1 Hz, 2H), 4.22 – 4.19 (m, 2H), 4.03 (ddd, J = 10.2, 5.5, 2.2 Hz, 1H), 3.82 (ddd, J = 15.1, 9.7, 8.9 Hz, 2H), 3.54 – 3.47 (m, 3H), 3.33 (dd, J = 10.1, 8.9 Hz, 2H), 3.25 (t, J = 7.6 Hz, 2H), 3.12 (s, 6H), 2.66 (t, J = 7.6 Hz, 2H), 2.52 (s, 3H), 2.34 (t, J = 7.4 Hz, 2H), 2.28 (s, 3H), 1.84 (p, J = 7.1 Hz, 2H), 1.61 (p, J = 7.3 Hz, 2H), 1.31 – 1.23 (m, 20H) ppm; ^{13}C NMR (126 MHz, CD3OD) δ 174.1, 173.2, 160.0, 155.1, 153.3, 144.9, 144.4, 143.4, 135.2, 134.3, 133.5, 128.1, 128.0, 125.0, 124.4, 122.7, 121.6, 120.0, 116.3, 111.2, 94.0, 93.9, 73.2, 72.9, 72.1, 71.9, 71.8, 70.8, 70.4, 70.2, 62.9, 49.9, 48.2, 48.0, 47.9, 47.2, 47.1, 40.8, 39.0, 34.3, 33.7, 29.9, 29.3, 29.2, 29.1, 28.9, 28.7, 28.7, 26.0, 24.7, 13.5, 9.8 ppm; HRMS (ESI-TOF+) calcd for $C_{59}H_{81}BF_2N_{10}O_{13}$ (M+H+) 1186.6155, found 1187.6128.

Synthesis of 6'-NH-DABCYL-2,3,4,2',3',4'-hexakis-O-(trimethylsilyl)-α,α-trehalose **3**

DABCYL-OH (62 mg, 0.23 mmol), EDC•HCl (51mg, 0.26 mmol), DMAP (2.7 mg, 0.02 mmol), and HOBt (41 mg, 0.26) were dissolved in dry CH_2Cl_2 (1 mL) and stirred at rt for 15 min, then cooled to 0°C. A solution of compound **2** (187 mg, 0.22 mmol) in dry CH_2Cl_2 (6 mL) was added dropwise via cannula,

and the reaction mixture kept at 0°C with slow addition of DIPEA (192 µL). Reaction was allowed to warm to rt for 20 h and then concentrated under reduced pressure and resuspended in CH_2Cl_2 (20 mL) and a cooled solution of 0.2 M Na_2CO_3/$NaHCO_3$ buffer pH=9 (20 mL). The crude reaction mixture was immediately transferred to a separatory funnel extracted with CH_2Cl_2, washed with brine, and dried over Na_2SO_4 to afford crude material. Purification of the resulting residue by column chromatography (SiO_2, 0→8% EtOAc/ CH_2Cl_2) afforded the title compound **3** (150 mg, 66%) as an orange solid: R_f = 0.35 (30% EtOAc/hexanes); ^{1}H NMR (400 MHz, $CDCl_3$) δ 7.75 – 7.73 (m, 2H), 7.71 – 7.73 (m, 4H), 6.61 – 6.60 (m, 2H), 6.30 (d, J = 3.1 Hz, 2H), 4.81 (d, J = 2.4 Hz, 1H), 4.75 (d, J = 3.7 Hz, 1H), 3.82 (dq, J = 8.4, 2.7 Hz, 1H), 3.80 (t, J = 8.9 Hz, 1H), 3.78 (t, J = 8.9 Hz, 1H), 3.75 (dt, J = 9.5, 3.4 Hz, 1H), 3.33 – 3.29 (m, 3H), 3.26 – 3.20 (m, 3H), 2.95 (s, 6H), 1.42 (dd, J = 7.4, 5.3 Hz, 1H), 0.04 (s, 9H), 0.00 (s, 9H), 0.00 (s, 9H), -0.01 (s, 9H), -0.01 (s, 9H), -0.11 (s, 9H) ppm; ^{13}C NMR (101 MHz, CDCl3) d 166.7, 154.9, 152.7, 143.5, 134.4, 127.7, 125.3, 122.1, 111.4, 94.2, 93.8, 73.9, 73.2, 73.1, 73.0, 72.9, 72.7, 72.6, 71.3, 61.6, 41.4, 40.2, 0.94, 0.91, 0.75, 0.23, 0.00, 0.00 ppm; HRMS (ESI-TOF+) calcd for $C_{45}H_{84}N_4O_{11}Si_6$ (M+H+) 1025.4825, found 1025.44830.

Synthesis of 6-O-(15-azidopentadeconyl)-6'-NH-DABCYL-2,3,4,2',3',4'-hexakis-O- (trimethylsilyl)-α,α-trehalose **4**

15-Azidopentadecanoic acid (23 mg, 0.082 mmol), EDC•HCl (31 mg, 0.164 mmol) and DMAP (6 mg, 0.049 mmol) were dissolved in dry CH_2Cl_2 (0.5 mL) and stirred at rt for 15 min. A solution of compound **3** (42 mg, 0.041 mmol) in dry CH_2Cl_2 (1 mL) was added dropwise via cannula, and the reaction mixture stirred at rt for 16 h and then concentrated under reduced pressure. Purification of the resulting residue by column chromatography (SiO_2, 0→4% EtOAc/hexanes) afforded the title compound **4** (36 mg, 69%) as an orange solid: R_f = 0.33 (10% EtOAc/hexanes); ^{1}H NMR (400 MHz, $CDCl_3$) δ 7.74 (m, 2H), 7.72 – 7.67 (m, 4H), 6.61 – 6.58 (m, 2H), 5.13 (t, J = 3.6 Hz, 2H), 4.82 (dd, J = 12.0, 2.4 Hz, 1H), 4.17 (ddd, J = 11.2, 7.9, 2.8 Hz, 2H), 3.91 – 3.72 (m, 5H), 3.31 (t, J = 9.0 Hz, 1H), 3.27 – 3.21 (m, 3H), 3.08 (t, J = 7.0 Hz, 2H), 2.94 (s, 6H), 2.19 (td, J = 7.5, 3.5 Hz, 2H), 1.48 – 1.39(m, 4H), 1.20 – 1.08 (m, 20H), 0.04 (s, 9H), 0.00 (s, 9H), -0.01 (s, 9H), -0.01 (s, 9H), -0.03 (s, 9H), -0.12 (s, 9H) ppm; ^{13}C NMR (101 MHz, CDCl3) δ 172.7, 165.7, 154.0, 151.7, 142.6, 133.5, 133.4, 126.8, 124.3, 121.2, 110.4, 72.9, 72.5, 72.3, 72.2, 72.0, 71.8, 71.7, 71.5, 70.8, 70.4, 70.1, 69.8, 62.2, 61.3, 52.4, 50.4, 40.5, 39.2, 33.1, 28.6, 28.5, 28.4, 28.4, 28.3, 28.1, 28.1, 27.8, 25.6, 23.7 0.00, 0.00, 0.00, -0.18, -0.88, -0.94 ppm; HRMS (ESI-TOF+) calcd for $C_{60}H_{111}N_7O_{12}Si_6$ (M+H+) 1290.6979, found 1290.6980

Synthesis of 6-O-(15-[BODIPY-FL]-pentadeconyl)-6'-NH-DABCYL-2,3,4,2',3',4'-hexakis-O-(trimethylsilyl)-α,α-trehalose **5**

Compound **4** (12 mg, 0.009 mmol) and BODIPY-FL alkyne (3 mg, 0.009 mmol) were dissolved in 5:5:1 t-BuOH:H_2O:CH_2Cl_2 (1.5 mL total). To this solution were added TBTA (97 µg in 96.7 µL CH_2Cl_2, 0.0018 mmol), sodium ascorbate (18 µL of a 0.1M aqueous solution, 0.0018 mmol), and $CuSO_4$•$5H_2O$ (9 µL of a 0.1M aqueous solution, 0.0009 mmol). The resulting mixture was stirred vigorously in the dark for 48 h, and then concentrated under reduced pressure. Purification of the resulting residue by column chromatography (SiO2, 40→90% EtOAc/hexanes) afforded the title compound **5** (11.2 mg, 76%) as an orange solid: R_f = 0.15 (50% EtOAc/hexanes); ^{1}H NMR (500 MHz, $CDCl_3$) δ 7.74 – 7.67 (m, 2H), 7.70 – 7.67 (m, 4H), 7.10 (s, 1H), 6.90 (s, 1H), 6.68 (d, J = 4.0 Hz, 1H), 6.60 (d, J= 4 Hz, 1 H), 6.31 – 6.29 (m, 2H), 6.07 (m, 1H), 5.95 (s, 1H), 4.82 (dd, J = 5.2, 3.1 Hz, 2H), 4.75 (dd, J = 11.9, 2.4 Hz, 1H), 4.32 (d, J = 5.8 Hz, 2H), 4.17 – 4.09 (m, 4H), 3.96 (dt, J = 9.5, 3.0 Hz, 1H), 3.90 (dd, J = 11.8, 4.5 Hz, 1H), 3.88 (ddd, J = 9.6, 4.5, 2.3 Hz, 1H), 3.81 (t, J = 8.9 Hz, 1H), 3.80 (t, J = 8.9 Hz, 1H), 3.75 (t, J = 9.1 S4 Hz, 1H), 3.33– 3.23 (m, 3H), 3.22 (t, J = 7.5 Hz, 2H), 2.94 (s, 6H), 2.48 (t, J = 7.6 Hz, 2H), 2.39 (s, 3H), 2.23 – 2.15 (m, 2H), 2.08 (s, 3H), 1.69 (q, J = 7.3 Hz, 2H), 1.46 – 1.43 (m, 4H), 1.13 – 1.07 (m, 18H), 0.04 (s,

9H), 0.00 (s, 9H), -0.01 (s, 9H), -0.01 (s, 9H), 0.03 (s, 9H), -0.12 (s, 9H) ppm; ^{13}C NMR (126 MHz, $CDCl_3$) δ 172.7, 170.2, 165.7, 159.4, 156.0, 154.0, 151.8, 142.9.9, 142.6, 134.2, 133.4, 132.3, 127.0, 126.8, 124.4, 122.7, 121.2, 121.0, 119.5, 116.2, 110.4, 93.1, 92.7, 72.9, 72.0, 71.8, 71.5, 70.8, 70.3, 69.8, 62.2, 49.3, 40.5, 39.3, 34.8, 34.0, 33.1, 29.2, 28.7, 28.6, 28.5, 28.4, 28.4, 28.3, 28.1, 28.0, 25.5, 23.8, 13.9, 13.2, 13.1, 10.3, 0.2, 0.0, -0.2, -0.2, -0.9, -0.9; HRMS (ESI-TOF+) calcd for $C_{77}H_{129}BF_2N_{10}O_{13}Si_6$ [(M+2H+)/2] 810.4281, found 810.4282

Fig. S1.

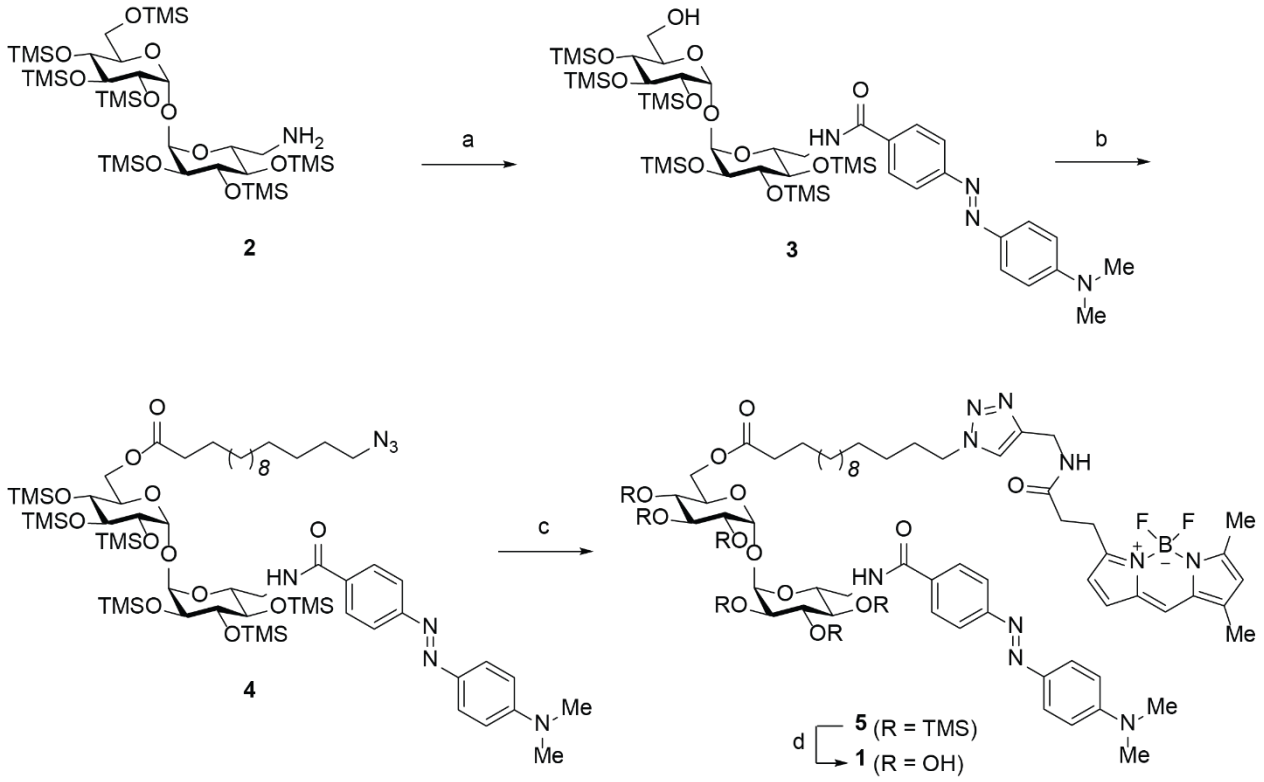

Synthetic scheme for the preparation of N-QTF. Reagents and conditions: a) DABCYL-OH, EDC•HCl, DMAP, HOBt, CH_2Cl_2, rt, 16 h, 66% b) 15-azidopentadecanoic acid, EDC•HCl, DMAP, CH_2Cl_2, rt, 16 h, 69%; c) BODIPY-FL-alkyne, $CuSO_4$•$5H_2O$, sodium ascorbate, TBTA, t-BuOH:H_2O:CH_2Cl_2 (5:5:1), rt, 24 h, 76%; d) Dowex-H+, MeOH, rt, 15 min 62%.

Fig. S2.

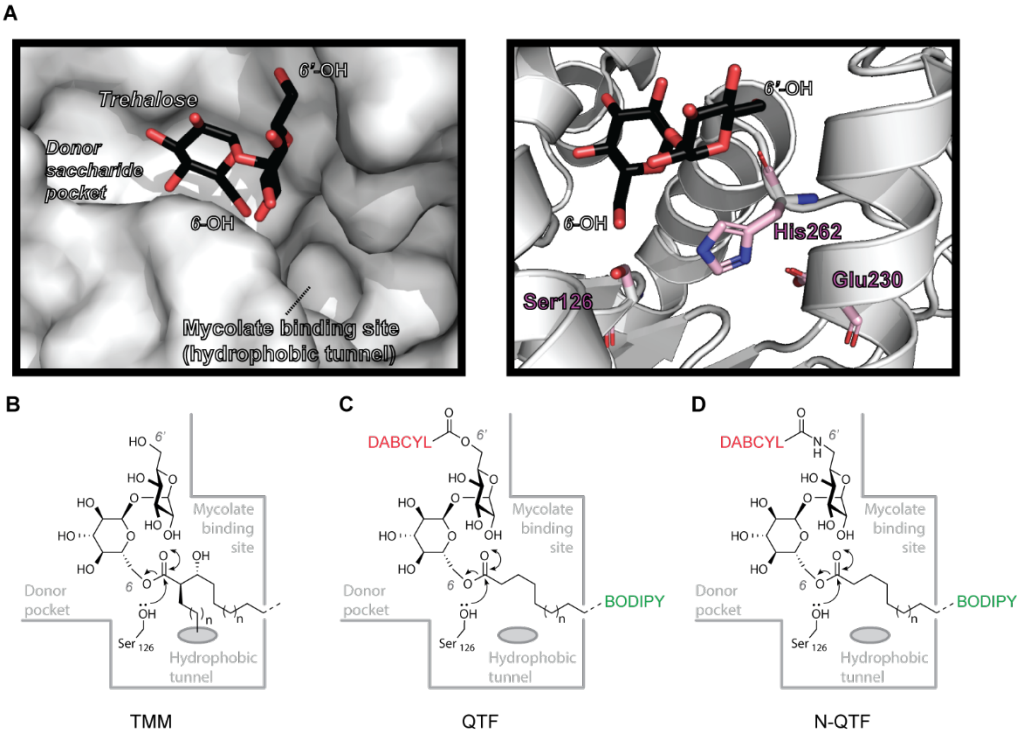

Substrate design. Substrate mimics were designed by leveraging the binding mode of the native substrate of antigen 85(*30*). (A) Left: Trehalose is shown proximal to the mycolate binding site to yield the trehalose monomycolate (TMM) substrate. Right: The catalytic triad residues (pink) Ser126, His262, and Glu230 are positioned next to the trehalose substrate for fatty acyl transfer. PDB: 1F0P (B) Mechanism of acyl transfer by the nucleophilic serine residue. (C) QTF substrate mimic predicts an analogous mechanism. (D) N-QTF increases the thermodynamic stability of the C6'-DABCYL-linked motif.

Fig. S3.

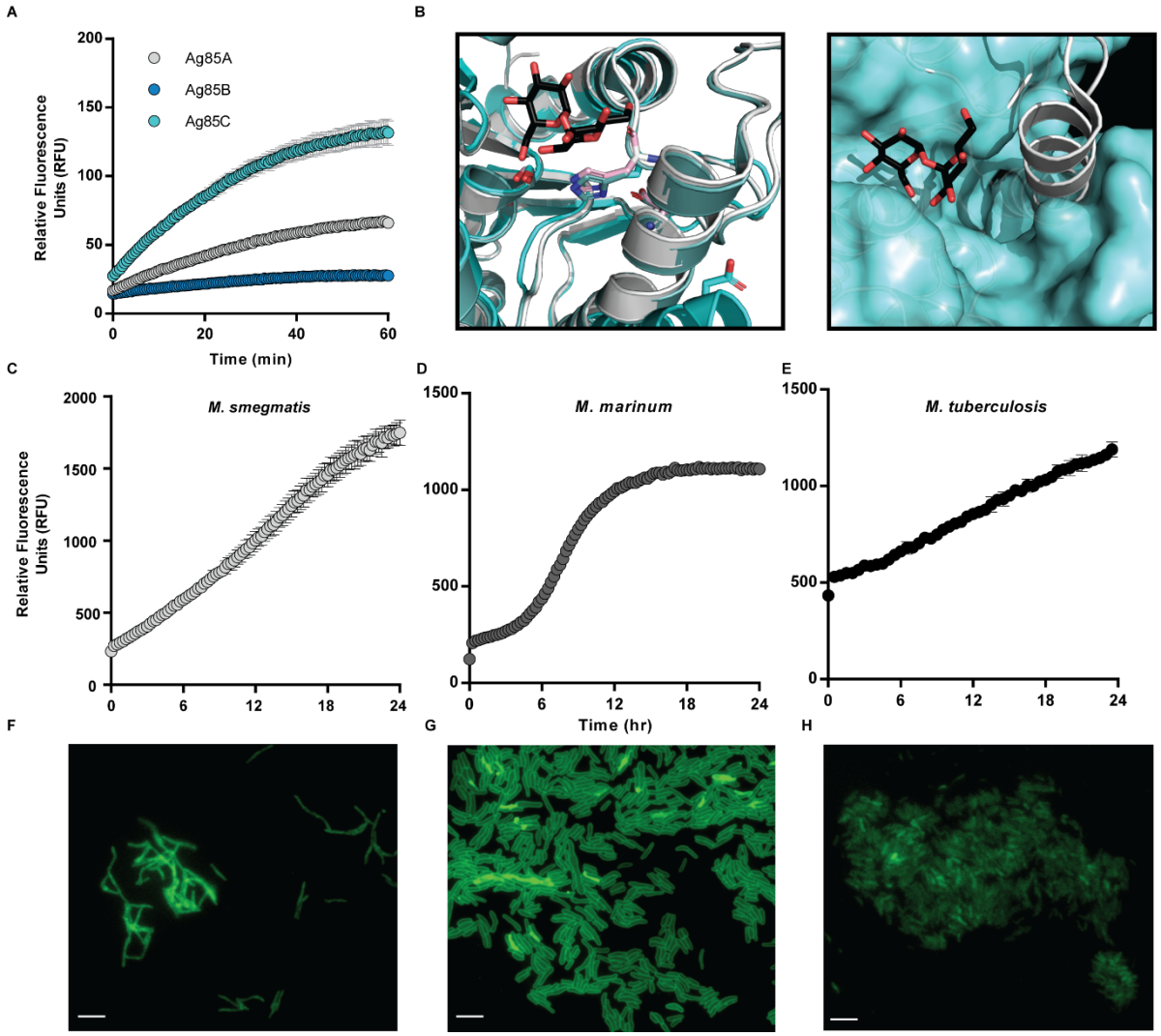

N-QTF activation by Antigen85 complex and Mycobacterial species. N-QTF (5 μM) activation by (A) antigen 85A (fbpA, Rv3804c, gray), antigen 85B (fbpB, Rv1886c, marine), and antigen 85C (fbpD, Rv3803, cyan). (B) Left: Structural alignment of Ag85A-C show conservation of catalytic cysteine and histidine residues. Right: overlay of Ag85A (PDB: 1F0P, gray) and Ag85C (PDB: 4MQM, cyan) shows an expanded hydrophobic tunnel(*31*). Incorporation of N-QTF over time and endpoint visualization in mycobacterial species (C, F) *M. smegmatis* (D, G) *M. marinum* and (E, H) *Mtb*. Scale bar 5 μm.

Fig. S4.

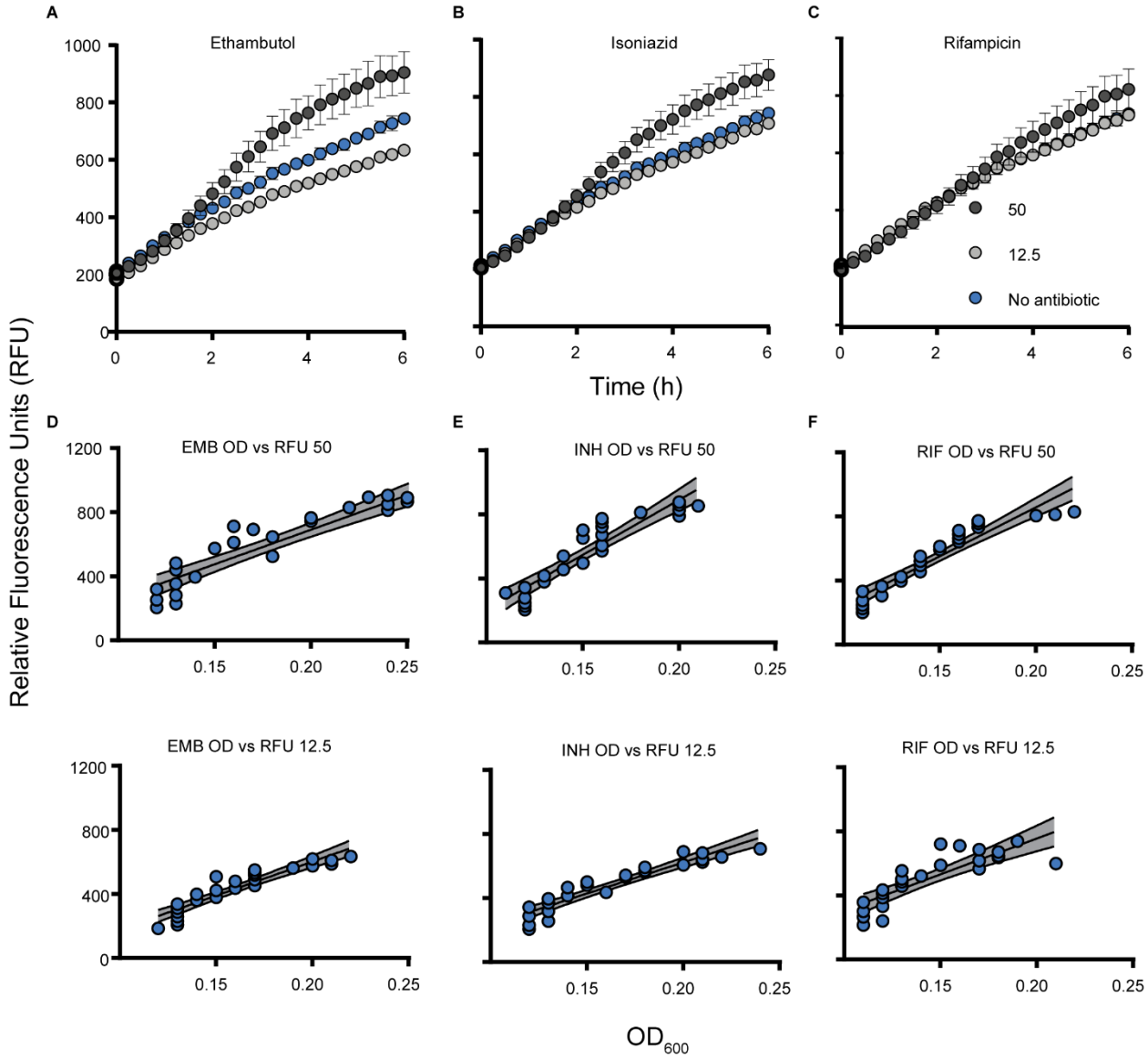

Fluorescence activation over time with frontline antibiotic treatment. Time-dependent changes in N-QTF treatment in the presence of frontline antibiotics (A) ethambutol (EMB), (B), isoniazid (INH), and (C) rifampicin (RIF) at 50 µg/mL (slate), 12.5 µg/mL (grey), and vehicle control (blue). Linear correlation plots of optical density (OD_{600}) vs relative fluorescence units (RFU) upon (D) EMB, (E) INH, and (F) RIF treatment at 50 µg/mL (top) and 12.5 µg/mL (bottom) antibiotic concentration.

Fig. S5.

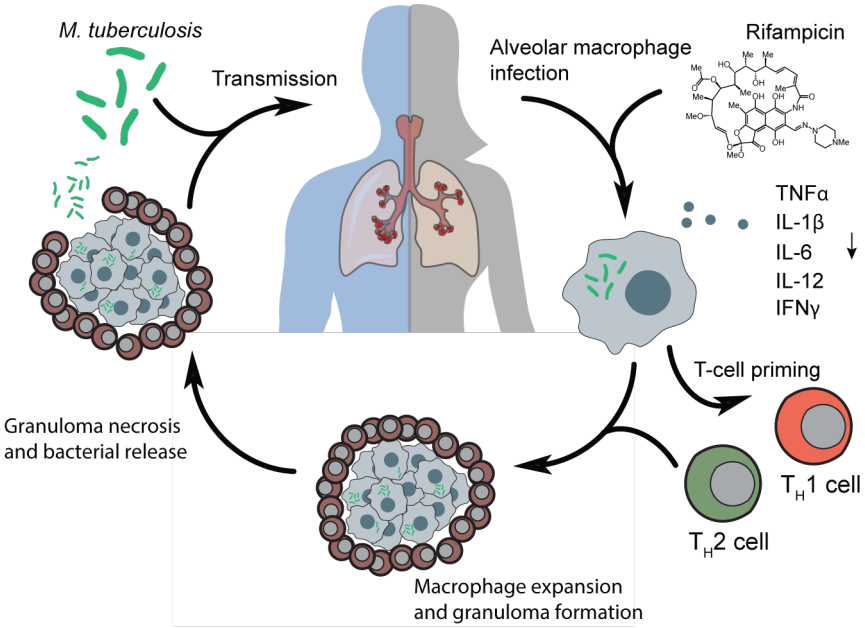

Mechanism of immune modulation following rifampicin treatment. *M. tuberculosis* infection cycle. Transmission and infection into human alveolar macrophages induces a proinflammatory immune response in normal clearance. Rifampicin-treatment induces the secretion of outer membrane vesicles that modulates macrophages which affects immune cell recruitment.

Table S1. Real time qPCR primer sequences

Gene	Gene ID	Forward Primer	Reverse Primer
Il-1b	**3553**	CACCTGTACGATCACTGAACTG	ACCACTTGTTGCTCCATATCC
IL-6	**3569**	TGCAATAACCACCCCTGACC	TGCGCAGAATGAGATGAGTTG
IL-12a	**3592**	TGAGCTATCTGAATGCTTCCTAAA	CCCTAGTTCTTAATCCACATCCTATC
IL-12b	**3593**	CACAGGAGGATGACACAGAAA	ACAATTTCATGTCCTTAGCCATAAC
TNFa	**7124**	AGAGGGAGAGAAGCAACTACA	GGGTCAGTATGTGAGAGGAAGA
IFNa	**3439**	AGGAATAACATCTGGTCCAACAT	TCAGTTTATCAGCATGGTCATAGTT
IFNb	**3456**	GCCGCATTGACCATCTATGA	GCCAGGAGGTTCTCAACAATAG
IFNg	**3458**	GGGTTCTCTTGGCTGTTACT	GAGTTCCATTATCCGCTACATCT
GAPDH	**2597**	CCATGTTCGTCATGGGTGTG	GGTGCTAAGCAGTTGGTGGTG

Table S2. Area ratios of targeted polar metabalomics of OMVs

	DMSO OMV E1	DMSO OMV E2	DMSO OMV E3	OMV E1	OMV E2	OMV E3	DMSO OMV R1	DMSO OMV R2	DMSO OMV R3	OMV R1	OMV R2	OMV R3
ethylnicotinamide	0	0	0	0	0	0	0	0	0	0	0	0
2,3-BPG	0	0	0	0	0	0	0.013	0.017	0.022	0.022	0.021	0.019
2-aminoadipate	1.806	1.935	1.731	2.261	2.343	2.269	0.316	0.305	0	0	0.151	0.328
-hydroxyglutarate	1.867	2.104	1.742	1.928	2.053	2.118	5.235	4.113	4.379	5.791	5.264	5.628
2-oxoadipate	0	0	0	0	0	0	0	0	0	0	0	0
3-hydroxybutyrate	0	0.007	0	0.015	0.005	0.009	0	0	0	0.005	0	0
phosphoglycerate	0.007	0.005	0.006	0.004	0.008	0.006	0.01	0.011	0.012	0.023	0.021	0.025
ureidopropionate	0	0	0	0	0	0	0	0	0	0	0	0
yindole_3-acetate	0	0	0	0	0	0	0	0	0	0	0	0
phosphogluconate	0	0	0	0	0	0	0	0	0	0	0	0
acetoacetate	0	0	0	0	0	0	0	0	0	0	0	0
acetylcarnitine	0	0.01	0.008	0.006	0.004	0.014	0.007	0.005	0.003	0.001	0.005	0.009
acetyl-CoA	0	0	0	0	0	0	0	0	0	0	0	0
acetylserine	0.471	0.657	0.774	0.744	0.547	0.683	0.493	0.115	0.023	0.134	0.184	0.091
adenine	2.517	2.064	1.809	2.61	2.066	1.974	0.078	0.074	0.071	0.385	0.333	0.338
adenosine	0.086	0.08	0.07	0.116	0.092	0.087	0.05	0.045	0.051	0.303	0.386	0.311
ADP	0	0	0	0	0	0	0	0	0	0	0	0
ADP-ribose	0	0	0	0	0	0	0	0	0	0	0	0
AICAR	0	0	0	0	0	0	0	0	0	0	0	0
alanine	2.906	2.776	3.195	3.564	3.592	3.305	0.509	0.188	0.11	0.249	0.222	0.24
alanine_13C3-15N	0	0	0	0	0	0	0	0	0	0	0	0
allantoin	0	0	0	0	0	0	0	0	0	0	0	0
pha-ketoglutarate	0.22	0.292	0.297	0.208	0.219	0.262	0.522	0.482	0.444	3.093	1.429	1.463
alpha-lipoic_acid	0	0	0	0	0	0	0	0	0	0	0	0
AMP	0.161	0.151	0.182	0.156	0.177	0.176	0.303	0.26	0.269	0.438	0.342	0.389
anserine	0	0	0	0	0	0	0	0	0	0	0	0
arginine	0.086	0.091	0.108	0.116	0.111	0.102	0.162	0.038	0.016	0.067	0.084	0.062
ginine_13C6-15N4	0	0	0	0	0	0	0	0	0	0	0	0
argininosuccinate	0	0	0	0	0	0	0	0	0	0	0	0
asparagine	0.001	0.001	0.002	0.003	0.002	0.001	0.003	0.001	0	0.002	0.002	0.002
aspartate	0.173	0.211	0.317	0.239	0.215	0.208	2.934	2.966	2.96	3.08	2.955	3.033
partate_13C4-15N	0	0	0	0	0	0	0	0	0	0	0	0
ATP	0	0	0	0	0	0	0	0	0	0	0	0
beta-alanine	1.396	1.332	1.627	1.711	1.714	1.256	0.266	0.165	0.203	0.318	0.276	0.285
betaine	0.088	0.159	0.143	0.183	0.133	0.156	0.308	0.134	0.167	0.175	0.148	0.154
butyryl_carnitine	0	0	0	0	0	0	0	0	0	0	0	0
C5_carnitines	0	0	0	0	0	0	0	0	0	0	0	0
cAMP	0.03	0.024	0.022	0.01	0.008	0.009	0	0	0.002	0.02	0.017	0.017
bamoyl_aspartate	0	0	0	0	0	0	0.043	0.042	0.049	0.046	0.045	0.044
carnitine	0.024	0.036	0.042	0.049	0.051	0.076	0.05	0.024	0.014	0.015	0.032	0.037
carnosine	0	0	0	0	0	0	0	0	0	0	0	0
CDP	0	0	0	0	0	0	0	0	0	0	0	0
choline	0.68	0.857	0.696	0.891	0.769	0.896	0.831	0.38	0.34	0.573	0.58	0.525
cis-aconitate	0	0.007	0.006	0.006	0.006	0.008	0	0	0	0	0	0
citrate	115.567	127.041	124.947	125.454	128.045	118.281	66.324	61.571	68.467	87.937	88.961	93.224
citrulline	0.298	0.329	0.74	0.392	0.436	0.394	0.463	0.149	0.058	0.059	0.056	0.064
CMP	0.006	0.014	0.006	0.006	0	0.003	0.035	0.043	0.04	0.041	0.035	0.023
creatine	0.003	0.004	0.005	0.007	0.004	0.01	0.013	0.003	0	0	0.005	0.004
creatinine	0.01	0.01	0.007	0.015	0.01	0.007	0.03	0.01	0.004	0.005	0.008	0.009
CTP	0	0	0	0	0	0	0	0	0	0	0	0
cystathionine	0	0	0	0	0	0	0	0	0	0	0	0
cysteine	0	0	0	0	0	0	0	0	0	0	0	0
cystine	1.009	0	0	1.131	0.709	0.702	0	0.216	0	0	0.236	0.248
cytidine	0	0.001	0	0	0.001	0	0.003	0.001	0.001	0.002	0.001	0.004
cytosine	0.024	0.018	0.017	0.025	0.02	0.017	0.054	0.048	0.048	0.045	0.04	0.035
dihydrofolate	0	0	0	0	0	0	0	0	0	0	0	0
dihydroorotate	0.002	0.002	0	0	0.002	0	0.089	0.072	0.057	0.079	0.061	0.055
etone_phosphate	0	0	0	0	0	0	0.019	0.014	0.019	0.025	0.029	0.029
dTMP	0.009	0.012	0.012	0.011	0.014	0.014	0.042	0.046	0.048	0.057	0.046	0.041
dTTP	0	0	0	0	0	0	0	0	0	0	0	0
dUMP	0	0	0	0	0	0	0	0	0	0	0	0
rose_4-phosphate	0	0	0	0	0	0	0	0	0	0	0	0
F6P/G1P	0.287	0.356	0.348	0.282	0.358	0.345	0.373	0.361	0.396	0.459	0.432	0.457
FAD	0	0	0	0	0	0	0	0	0	0	0	0
folate	0	0	0	0	0	0	0	0	0	0	0	0
_1,6-bisphosphate	0	0	0	0	0	0	0	0	0	0	0	0
fumarate	0.296	0.327	0.265	0.271	0.309	0.392	0.225	0.201	0.278	0.252	0.288	0.193
GAR	0	0	0	0	0	0	0	0	0	0	0	0
GDP	0	0	0	0	0	0	0	0	0	0	0	0
glucose	0.752	0.584	0.473	0.744	0.501	0.538	0.614	0.463	0.483	0.629	0.497	0.524
cose_6-phosphate	0.222	0.206	0.218	0.22	0.234	0.216	0.671	0.608	0.667	0.813	0.816	0.819
glutamate	84.184	84.682	85.275	72.85	73.625	73.377	117.586	112.611	114.603	179.119	166.407	174.768
tamate_13C5-15N	0	0	0	0	0	0	0	0	0	0	0	0
glutamine	0.085	0.095	0.088	0.1	0.092	0.101	0.079	0.069	0.072	0.115	0.104	0.108
yde_3-phosphate	0	0	0	0	0	0	0.019	0.014	0.019	0.028	0.029	0.029
erol_3-phosphate	0.287	0.361	0.389	0.365	0.473	0.482	0.23	0.254	0.296	0.226	0.257	0.273
rophosphocholine	0.371	0.423	0.479	0.996	0.749	0.593	0.48	0.443	0.387	0.567	0.543	0.591
glycine	0	3.749	1.043	0	0.686	0	0	0	0	0.306	0	0
glycine_13C2-15N	0	0	0	0	0	0	0	0	0	0	0	0
GMP	0.065	0.064	0.074	0.066	0.072	0.073	0.052	0.042	0.052	0.073	0.072	0.082
GSH	1.067	0	0	1.539	0.472	0.401	0	0.378	0	0	0.476	0.461
GSSG	0	0	0	0	0	0	0	0	0	0	0	0
GTP	0	0	0	0	0	0	0	0	0	0	0	0

Table S2 continued

guanidinoacetate	0	0	0	0	0	0	0	0	0	0	0	0
guanine	0	0	0	0	0	0	0	0	0	0	0	0
guanosine	0.014	0.012	0.013	0.014	0.009	0.003	0.013	0.008	0.008	0.194	0.231	0.244
histidine	0.108	0.158	0.186	0.148	0.177	0.135	0.145	0.053	0	0.027	0.037	0.017
stidine_13C6-15N3	0	0	0	0	0	0	0	0	0	0	0	0
homocysteine	0	0	0	0	0	0	0	0	0	0	0	0
hydroxyproline	0.002	0.002	0.002	0.003	0.002	0.002	0.001	0.001	0.001	0.001	0	0.001
hypotaurine	0	0	0	0	0	0	0	0	0	0	0	0
hypoxanthine	0.506	0.446	0.393	0.548	0.444	0.445	0.26	0.244	0.225	0.282	0.256	0.233
IMP	0	0	0	0	0	0	0.074	0.073	0.08	0.074	0.06	0.055
inosine	0	0	0	0	0	0	0	0	0	0	0	0
isoleucine	0.144	0.078	0.179	0.104	0.142	0.125	0.147	0.089	0.074	0.241	0.115	0.212
leucine_13C6-15N	0	0	0	0	0	0	0	0	0	0	0	0
itaconic_acid	0.517	0.523	0.563	0.512	0.549	0.555	0.484	0.409	0.427	0.477	0.4	0.429
kynurenic_acid	0	0	0	0	0.002	0	0.15	0.009	0	0	0	0
kynurenine	0	0	0	0	0	0	0	0	0	0	0	0
lactate	82.724	76.936	79.031	90.337	74.404	68.273	7.91	6.312	5.866	9.111	7.767	7.769
leucine	0.129	0.154	0.195	0.17	0.134	0.147	0.173	0.126	0.072	0.178	0.195	0.078
leucine_13C6-15N	0	0	0	0	0	0	0	0	0	0	0	0
lysine	1.038	1.112	1.052	1.105	1.168	1.119	0.129	0.088	0.064	0.188	0.196	0.166
lysine_13C6-15N2	0	0	0	0	0	0	0	0	0	0	0	0
malate	0.626	0.526	0.413	0.608	0.509	0.473	0.315	0.179	0.159	0.191	0.21	0.212
methionine	0	0	0	0	0	0	0	0	0	0	0	0
hionine_13C6-15N	0	0	0	0	0	0	0	0	0	0	0	0
thylthioadenosine	0.027	0.025	0.024	0.032	0.032	0.028	0	0	0.001	0.005	0.003	0.003
a_acetylglutamine	0	0	0	0	0	0	0.637	0.648	0.688	0.628	0.677	0.505
Na-acetylornithine	0.108	0.145	0.164	0.128	0.157	0.18	0.546	0.585	0.666	0.632	0.717	0.687
N-acetylcysteine	0	0	0	0	0	0	0	0	0	0	0	0
N-acetylglutamate	0.064	0.087	0.086	0.066	0.09	0.088	0.307	0.269	0.314	0.316	0.307	0.364
-acetylmethionine	0	0	0	0	0	0	0	0	0	0	0	0
cetylphenylalanine	0	0	0	0.001	0	0	0.007	0.006	0.005	0.007	0.008	0.005
NAD	0.009	0.01	0.003	0.009	0.01	0.011	0.017	0.014	0.009	0.038	0.038	0.043
NADH	0	0	0	0	0	0	0	0	0	0	0	0
NADP	0	0	0	0	0	0	0	0	0	0	0	0
NADPH	0	0	0	0	0	0	0	0	0	0	0	0
Ne-acetyllysine	1.14	1.504	1.664	1.416	1.876	1.671	0.77	0.94	1.195	1.088	1.127	1.355
nicotinamide	0.004	0.003	0.003	0.005	0.003	0.004	0.014	0.015	0.01	0.017	0.016	0.014
nicotinic_acid	12.087	9.806	8.594	12.859	10.448	9.991	0.043	0.039	0.039	0.06	0.05	0.05
ornithine	0	0	0.045	0	0.02	0	0.036	0	0	0	0.025	0
orotate	0.002	0.003	0	0.005	0.001	0	0.134	0.125	0.095	0.138	0.125	0.079
palmitate	2.992	1.47	1.064	10.07	3.147	2.84	0.091	0.028	0.024	0.027	0.024	0.109
pantothenic_acid	0.346	0.339	0.424	0.367	0.368	0.362	1.858	1.928	2.157	1.741	1.657	1.73
/acetyl_glutamine	0	0	0	0	0	0	0	0	0	0	0	0
phenylalanine	1.621	1.522	1.481	1.775	1.651	1.572	0.181	0.142	0.133	0.201	0.186	0.182
lalanine-13C9-15N	0	0	0	0	0	0	0	0	0	0	0	0
phosphocholine	0.583	0.626	0.708	0.767	0.857	0.741	0.026	0.015	0.007	0.044	0.021	0.048
phosphocreatine	0	0	0	0	0	0	0	0	0	0	0	0
sphoenolpyruvate	0.004	0.005	0.005	0.007	0.005	0.008	0.11	0.121	0.136	0.15	0.147	0.15
phoethanolamine	0.094	0.079	0.085	0.097	0.117	0.112	0	0	0	0	0	0
phosphoserine	0	0	0	0	0	0	0	0	0	0	0	0
pipecolic_acid	0.001	0	0	0.001	0.002	0.001	0.001	0	0.002	0.002	0.001	0.001
proline	1.117	1.104	1.127	1.254	1.229	1.217	0.098	0.048	0.037	0.042	0.051	0.045
proline_13C5-15N	0	0	0	0	0	0	0	0	0	0	0	0
propionylcarnitine	0	0	0	0	0	0	0	0	0	0	0	0
PRPP	0	0	0	0	0	0	0	0	0	0	0	0
pseudouridine	0.001	0.001	0	0.001	0.001	0.001	0	0	0	0.001	0	0
pyruvate	0.313	0.274	0.277	0.337	0.284	0.254	0.019	0	0	0.019	0	0
lose_5-phosphate	0.004	0.008	0.011	0.014	0.021	0.022	0.068	0.074	0.08	0.085	0.105	0.093
bose_1-phosphate	0.082	0.078	0.085	0.083	0.098	0.086	0.104	0.076	0.088	0.119	0.111	0.137
saccharopine	0	0	0	0	0	0	0	0	0	0	0	0
osylhomocysteine	0	0	0	0	0	0	0	1.51	0	0	0	0
enosylmethionine	5.047	0	0	5.538	3.85	3.792	0	5.398	0	0	6.587	6.113
sarcosine	0	0	0	0	0	0	0	0	0	0	0	0
lose_7-phosphate	0.016	0.017	0.015	0.022	0.019	0.017	0.151	0.128	0.145	0.139	0.121	0.15
serine	0.115	0.226	0.855	0.27	0.225	0.166	1.121	0.214	0	0.082	0.271	0.145
serine_13C3-15N	0	0	0	0	0	0	0	0	0	0	0	0
S-methylcysteine	0	0	0	0	0	0	0	0	0	0	0	0
succinate	0.188	0.205	0.19	0.179	0.194	0.192	0.16	0.202	0.194	0.355	0.291	0.287
taurine	0.276	0	0	1.067	0.563	0.331	0	14.037	0	0	15.047	11.682
threonine	0.293	0.32	0.435	0.386	0.372	0.334	0.38	0.249	0.129	0.194	0.246	0.24
reonine_13C4-15N	0	0	0	0	0	0	0	0	0	0	0	0
tryptophan	0	0	0	0	0	0	0	0	0	0	0	0
tyrosine	0.479	0.525	0.585	0.584	0.58	0.573	0.2	0.156	0.154	0.19	0.188	0.212
yrosine_13C9-15N	0	0	0	0	0	0	0	0	0	0	0	0
UDP	0	0	0	0	0	0	0	0	0	0	0	0
UDP-GlcNAc	0	0	0	0	0	0	0	0	0	0	0	0
UDP-hexose	0	0	0	0	0	0	0.013	0.015	0.012	0.034	0.028	0.029
UMP	0.089	0.091	0.09	0.095	0.093	0.085	0.154	0.134	0.154	0.144	0.142	0.146
uracil	0.08	0.058	0.043	0.079	0.054	0.053	0.016	0.014	0.011	0.022	0.018	0.008
urate	0.042	0.091	0.028	0.048	0.035	0.031	0.272	0.158	0.167	0.459	0.374	0.374
uridine	0.012	0.006	0.006	0.012	0.009	0.007	0.006	0.005	0.006	0.006	0.007	0.005
UTP	0	0	0	0	0	0	0	0	0	0	0	0
valine	0.464	0.443	0.386	0.538	0.464	0.457	0.374	0.423	0.332	0.36	0.336	0.446
valine-13C5-15N	0	0	0	0	0	0	0	0	0	0	0	0
xanthine	0.321	0.27	0.2	0.369	0.252	0.252	0.107	0.079	0.074	0.089	0.09	0.077
xanthosine	0	0	0	0	0	0	0	0	0	0	0	0

Movie S1. Timelapse microscopy of N-QTF incorporation in *M. smegmatis*
Representative timelapse microscopy experiment of N-QTF incorporation into growing *M. smegmatis* mc2155 under constant flow of 7H9 medium and N-QTF. Images were acquired every 15 minutes. Images representative of this movie were compiled into Figure 2A.

Movie S2. Timelapse microscopy of N-QTF incorporation in *M. smegmatis* exposed to EMB
Representative timelapse microscopy experiment of N-QTF incorporation into growing *M. smegmatis* mc2155 under constant flow of 7H9 medium, N-QTF and then ethambutol treatment. Images were acquired every 15 minutes. Images representative of this movie were compiled into Figure 2B.

Movie S3. Timelapse microscopy of N-QTF incorporation in *M. smegmatis* exposed to INH
Representative timelapse microscopy experiment of N-QTF incorporation into growing *M. smegmatis* mc2155 under constant flow of 7H9 medium, N-QTF and then isoniazid treatment. Images were acquired every 15 minutes. Images representative of this movie were compiled into Figure 2C.

Movie S4. Timelapse microscopy of N-QTF incorporation in *M. smegmatis* exposed to RIF
Representative timelapse microscopy experiment of N-QTF incorporation into growing *M. smegmatis* mc2155 under constant flow of 7H9 medium, N-QTF and then rifampicin treatment. Images were acquired every 15 minutes. Images representative of this movie were compiled into Figure 2D.